

25p



X64

12605 *

Code 2

(NASA TM X-851)



NASA TECHNICAL MEMORANDUM



NASA TM X-851

Declassified by authority of NASA
Classification Change Notices No. 26
Dated **10-5-86

FREE-FLIGHT MEASUREMENTS OF RADIATIVE HEATING TO THE FRONT FACE OF THE APOLLO REENTRY CAPSULE AS A FUNCTION OF ANGLE OF ATTACK

by Edward E. Walters

Ames Research Center
Moffett Field, California

FACILITY FORM 602

| | |
|------------------------------------|------------|
| (ACCESSION NUMBER) | (FUND) |
| (PAGES) | (CODE) |
| (NASA CATALOG NUMBER OR AD NUMBER) | (CATEGORY) |

NATIONAL AERONAUTICS AND SPACE ADMINISTRATION • WASHINGTON, D. C. • NASA, FEBRUARY 1964



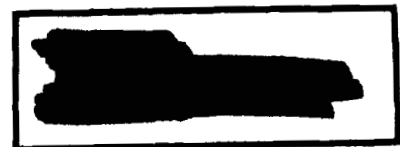
58
up

[REDACTED]
DECLASSIFIED

FREE-FLIGHT MEASUREMENTS OF RADIATIVE HEATING TO THE
FRONT FACE OF THE APOLLO REENTRY CAPSULE
AS A FUNCTION OF ANGLE OF ATTACK

By Edward E. Walters

Ames Research Center
Moffett Field, Calif.



DOCUMENT - UNCLASSIFIED



NATIONAL AERONAUTICS AND SPACE ADMINISTRATION



CONFIDENTIAL
FREE-FLIGHT MEASUREMENTS OF RADIATIVE HEATING TO THE

FRONT FACE OF THE APOLLO REENTRY CAPSULE

AS A FUNCTION OF ANGLE OF ATTACK*

By Edward E. Walters

SUMMARY

12605

A

The effect of angle of attack on the total equilibrium radiative heat load has been measured on a body similar to the Apollo command capsule. The measurements were made on models, approximately 0.4-inch diameter, flying through air at 23,000 and 35,000 ft/sec. The results of these tests show that as the angle of attack increases, the total radiation from the shock layer ahead of the model decreases.

The variation of shock-layer radiation with angle of attack agreed well with predicted values. At zero angle of attack, experimental and calculated values for the absolute magnitude of shock-layer radiation were in agreement.

Shock-wave shapes determined from shadowgraphs of the model in flight at 23,000 ft/sec were found to agree with predicted shock-wave shapes. The predicted shapes were employed in the flow-field calculations necessary for estimating radiation from the shock layer.

AUTHOR

Conf.


INTRODUCTION

On reentry, a blunt-nosed capsule at supercircular velocity must fly at angle of attack if lift is to be used to increase the reentry corridor depth. It is recognized that the angle of attack will affect the radiative heating of the capsule, but so far the extent of this effect has not been established experimentally. It is the purpose of this paper to present such experimental data, with supporting predictions, for a capsule shape similar to Apollo.

SYMBOLS

| | |
|---|---------------------------|
| A | area |
| D | function in equation (A5) |
| d | frontal model diameter |
| I | radiant intensity |

CONFIDENTIAL


 K_1, K_2 empirical coefficients in equation (A1)

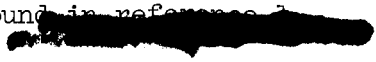

M_∞ Mach number
 p_∞ free-stream pressure
 T_∞ free-stream temperature
 V velocity
 W total radiation from the shock layer ahead of the model
 α angle of attack
 δ shock standoff distance normal to the body surface
 ρ_∞ free-stream density
 $\frac{\rho_1}{\rho_2}$ density ratio across a normal shock wave
 ϕ, θ, r spherical coordinates
 ψ angle between the velocity vector and a normal to the shock wave

Subscripts

B conditions on the body surface
ECL eclipsed
EL elemental
PS plane of shadow
S conditions on the shock wave
seen seen by the photomultiplier
 α angle of attack

FACILITY

The tests reported in this paper were performed in free flight in the prototype of the Ames Hypersonic Free-Flight Facility. Models were launched from a hypervelocity gun both into a countercurrent shock-driven hypersonic wind tunnel and into still air. A brief description of the major components of the facility is given below. A more detailed description may be found in reference 1.

A schematic view of the facility is shown in figure 1. The model launcher used for these tests was a caliber 0.50, deformable-piston, light-gas gun similar to the one described in reference 2. The instrumented test section consists of 11 shadowgraph stations spaced at 4-foot intervals along its length. An enlarged view of part of the test section is shown in the inset to figure 1. Shadowgraphs are taken in orthogonal planes perpendicular to the flight axis as the model passes each station. A typical shadowgraph of the present model configuration in flight is shown in figure 2. Time of firing of the individual shadowgraph sparks is recorded by electronic chronographs. The time-distance history and angle-of-attack and yaw histories of the model are extracted from the shadowgraph pictures and chronograph records.

When this facility is used as a free-flight wind tunnel, the air stream is supplied from a 40-foot-long, 6-1/4-inch-diameter shock tube driven by a combustion chamber of like dimensions. The energy for driving the shock tube is supplied by the constant volume combustion of H_2 and O_2 diluted with He and N_2 . The shock-tube diaphragm is broken when the combustion chamber has reached peak temperature and pressure. The resulting shock compresses the air in the driven section. The initial pressure in the driver section is adjusted to tailor the reflected shock at the interface (ref. 1). The high-pressure, high-temperature air produced by the double shock process is expanded through an $M = 7$ contoured nozzle to provide the air stream.

MODELS AND TEST CONDITIONS

Figure 3 is a dimensioned sketch of the models used in these tests. The nose shape and afterbody half-angle were patterned after the Apollo capsule and differ from it only in minor details, as shown in the figure. These models were fabricated of aluminum or Teflon.

A two-piece split sabot machined from Lexan polycarbonate plastic was used to fit the model to the launch tube of the gun. A picture of a model in its sabot is shown in figure 4.

Tests were carried out at two nominal test conditions. These are summarized in the following table:

| | | |
|--|---|---|
| Test velocity | 23,000 ft/sec | 35,000 ft/sec |
| Model velocity | 23,000 ft/sec | 23,000 ft/sec |
| Air-stream velocity | 0 | 12,000 ft/sec |
| ρ_∞ | 1.9×10^{-4} slug/ft ³ | 2.3×10^{-5} slug/ft ³ |
| p_∞ | 167 lb/ft ² | 60 lb/ft ² |
| M_∞ | 20.6 | 18.4 |
| T_∞ | 519° R | 1500° R |
| Model material | 7075-T6 Al alloy | Teflon |
| Reynolds number based on model frontal diameter and free-stream properties | 390,000 | 40,000 |

Measurements were made of (1) the position and attitude of the model with respect to each radiation-measuring station, (2) the model velocity at each radiation-measuring station, (3) the free-stream properties of the air which was the models' flight environment, and (4) the total radiation emitted from the shock layer ahead of the model.

Measurements of model position, attitude, and velocity were made with the standard ballistic-range techniques already outlined. The measurements and calculations necessary to determine the free-stream properties and the shock-layer radiation from the model will be described in detail in this section.

Free-Stream Properties

For the tests at 23,000 ft/sec in which the models were fired into still air, the free-stream properties were determined from the measured pressure and temperature of the air in the tunnel immediately prior to the firing of each shot. For the tests at 35,000 ft/sec, in which models were fired into the supersonic air stream, free-stream properties were determined by the following technique.

Wind-tunnel reservoir properties were determined by measuring (1) the pressure and temperature of the air in the shock tube prior to the run, (2) the shock velocity, and (3) the pressure behind the reflected shock wave (the stagnation pressure driving the wind tunnel). From these measurements the stagnation conditions for the wind-tunnel reservoir were calculated by applying the appropriate shock-tube equations, which may be found in any standard gasdynamics text (e.g., ref. 3). Wind-tunnel free-stream properties were then determined from the static pressure measured at several points on the test-section wall. The real-gas flow between the reservoir and the test section was assumed to be isentropic and in equilibrium. A probe mounted in the tunnel during calibration tests showed pitot pressures consistent with predictions based on the above measurements.

Gas-Cap Radiation Measurements

The radiometers depicted schematically in figures 1 and 5 consisted of six S-5 spectral-response photomultipliers (type RCA 1P28) calibrated by the method outlined in reference 4. These tubes were mounted in housings on the test section walls. They were placed in pairs in orthogonal viewing lines to give two readings for a given model run and attitude. A series of half-inch-wide slits limited the field of view of the photomultipliers. The output signals from the tubes were recorded by fast-rise oscilloscopes. A typical oscilloscope record is shown in figure 6.

In order to keep the response of the photomultipliers well within their linear range, etched metal screens, such as the one shown in figure 7, were used

[REDACTED]

as neutral density optical filters to reduce the intensity of radiation incident on the photocathodes. These screens were optically calibrated for their light transmission.

The radiation data from this instrumentation were reduced in several steps:

- (1) The output of the photomultiplier tubes was read from the oscilloscope records. (The cause of the small oscillations at the peak of the phototube output (see fig. 6) has not been determined. They do not appear on all records.)
- (2) This output was multiplied by the calibration constant for the tube, which was adjusted by the inverse square law, to correspond to the distance of the model from the tube to give the number of "watts seen."
- (3) A correction was then applied to account for the difference between the spectral energy distribution of the radiation in the model shock layer and the spectral sensitivity of the phototube. The tube responded to approximately 70 percent of the total radiation at 23,000 ft/sec and approximately 50 percent at 35,000 ft/sec.
- (4) A geometric correction was then applied. If the radiating shock layer is partially obscured by the body of the model as it passes the phototube, the tube cannot measure all the radiation from the shock layer. This shadowing effect depends on the angle of attack and on the roll attitude of the model with respect to the photomultiplier. The roll angle is determined by projecting the axis of symmetry of the model onto the plane normal to the flight direction and is the angle between this projection and the optical axis of each radiation measuring station. A diagram of this projection is shown in figure 8. The correction factor (roll-angle eclipsing factor) was formed by computing the fraction of the total radiation visible to the photomultiplier for each individual data point. A detailed description of the procedure is given in appendix A. The magnitude of the correction was, on the average, about 0.7. Its validity can be inferred from the data and will be discussed in the section on Results and Discussion.

In summary, it was necessary to apply a correction for spectral sensitivity of the phototube and a correction for geometric effect to the "watts seen" data to obtain W , the total radiation from the gas cap at angle of attack.

RESULTS AND DISCUSSION

The results of these experiments are presented in figures 9 and 10. Each value of W measured has been normalized to the value of W predicted for its particular test conditions. This eliminates scatter in the data due to slight changes in test velocity and density from run to run. The predictions of reference 5 were used for this normalization. In addition, the normalized values of W thus obtained were divided by the measured normalized value of W at small α to produce the data shown on figures 9 and 10.

The symbols in figure 9 represent the data obtained at a nominal velocity of 23,000 ft/sec. The test conditions were chosen so that the gas-cap radiation was from equilibrium air, as shown by the measurements of reference 6. It can be seen that $W/W_{\alpha=0}$ decreases with increasing angle of attack, reaching a value of about 0.4 at $\alpha = 30$.

[REDACTED]

[REDACTED]

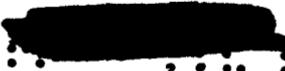
These data exhibit low scatter for an experiment of this type. This can be traced to two probable causes. First, the models for this speed were made of aluminum which did not ablate, so that the radiation measured was from air uncontaminated by ablation products. Second, the free-stream properties were easily and accurately measured, so less perturbation was introduced as a result of imprecise knowledge of free-stream velocity and density.

In addition to the experimental data points, a curve is shown on figure 9 which gives the results of calculations made to determine the effect of angle of attack on $W/W_{\alpha=0}$. This curve was computed from shock shapes deduced by the methods of reference 7. The equilibrium theory of reference 5 was then used to compute the radiation at various points behind the shock and on the body surface. This curve and the experimental data agree well. More detail on the method for calculating this curve will be found in appendix A.

Figure 10 presents the data obtained for a velocity of 35,000 ft/sec. Again the radiation was from air in equilibrium. These data exhibit more scatter than the data from the lower velocity tests, probably because of the unknown effect of ablation from the Teflon model and the poorer definition of free-stream conditions. Also less data were obtained for these conditions so a curve defined by the data is not as clear. However, there are sufficient data to indicate the same sort of reduction of $W/W_{\alpha=0}$ with increasing angle of attack as was shown for the 23,000 ft/sec tests.

A prediction of $W/W_{\alpha=0}$ was also made for these test conditions. A comparison of the two curves shows that the predicted variation of radiation with α is essentially the same for the two speeds. As is shown in references 8 and 9, this agreement can be expected to hold within a few percent over a wide range of flight conditions. As a part of the predictions of $W/W_{\alpha=0}$ versus α it was necessary to determine the radiation which should have been seen at these test conditions for $\alpha = 0$. The equilibrium predictions of reference 5 were used to compute this value. The absolute value of the test results for $\alpha = 0$, that is, $W_{\alpha=0}$, agrees with these calculations within 20 percent. The data also agree well with the experimental data of reference 6 for these test conditions.

The success of the roll-angle eclipsing correction, described in the section on measurements, can be inferred from figures 9 and 10. It will be noted that on these figures, there are, in most cases, pairs of values for $W/W_{\alpha=0}$ at the same angle of attack. These pairs are from simultaneous measurements taken by two photomultipliers viewing the model from different directions (see fig. 8). Thus the two values for $W/W_{\alpha=0}$ from the same pair, corrected to account for the radiation hidden from the tube by the model, should be identical. It can be seen from the figure that these two values from each pair do lie reasonably close to one another. Furthermore, it was found, during the course of data reduction, that the eclipsing correction invariably improved the agreement between simultaneous readings. Thus it is believed that these corrections were valid.


Comparison of Experimental and Predicted
Shock Shapes


During the course of the experiment, several shadowgraphs were obtained which clearly showed the shock-wave shapes. One shape observed is compared with a predicted shape in figure 11 and serves to support the calculations of $W/W_{\alpha=0}$ and the roll-angle eclipsing corrections applied to the data (see appendix A).

The method for computing the shock-wave shape (ref. 7) was derived empirically from data taken at much lower Mach numbers and density ratios than were obtained during the present tests. However, the method was believed to be applicable at the higher Mach numbers, and the evidence obtained from the present shadowgraphs supports this belief.

CONCLUSIONS

1. It was shown experimentally that for a reentry capsule, shaped like the Apollo configuration, the total equilibrium radiative heat load on the front face decreases as the angle of attack increases. This decrease is such that at a lift-to-drag ratio of about $1/2$, $\alpha = 30^\circ$, the total equilibrium radiative heat load is about 40 percent of the value for $\alpha = 0^\circ$.
2. The experimental results agree well with calculations made for the variation of radiative heat load with angle of attack. In the calculations the shock layer was assumed to have equilibrium properties.
3. For values of α near zero, the absolute value of the experimentally observed total radiation from the shock layer is very nearly that predicted for equilibrium conditions on the basis of earlier shock tube and theoretical studies.
4. As a corollary to the experiment, comparisons were made between the calculated shock shapes used in computing the total gas-cap radiation and shapes derived directly from experimental shadowgraphs. Agreement between the two was quite good.

Ames Research Center
National Aeronautics and Space Administration
Moffett Field, Calif., Oct. 21, 1963



PREDICTION OF RADIATIVE HEATING AS A FUNCTION OF ANGLE OF ATTACK

The first step in the analysis was to determine the shape of the bow shock wave as a function of angle of attack at the test conditions. Reference 7 presents a correlation method for determining shock shapes on blunt axisymmetric bodies at angle of attack. Some results of reference 7 are reproduced in a simplified form on figure 12, where the solid line is the correlation curve which was derived from data on the Apollo vehicle at low supersonic Mach numbers. Comparison of this correlation with shock shapes from the present experiment shows that, as expected, this correlation applies to the present high Mach number shock shape data as well (see fig. 11).

To facilitate computation the correlation curve was fitted with an equation of the form

$$K_1\theta + K_2\theta^3 = \frac{\rho_2}{\rho_1} \frac{(\delta/d)_\alpha - (\delta/d)_{\alpha=0}}{\sin \alpha \cos \varphi} \quad (A1)$$

where the coordinate system is defined in the inset to figure 12. In addition, ρ_1/ρ_2 is the density ratio across a normal shock and δ/d is the diameter-normalized stand-off distance measured perpendicular to the body surface.¹ The constants in equation (A1) were determined to be $K_1 = -1.85$ and $K_2 = -3.79$. The points thus fitted to the correlation curve are shown as circles on figure 12. Equation (A1) was solved for

$$\delta_\alpha = d \frac{\rho_1}{\rho_2} \sin \alpha \cos \varphi (K_1\theta + K_2\theta^3) + \delta_{\alpha=0} \quad (A2)$$

Next, the above equation was used to write an equation for the shock-wave shape:

$$0 = D = -r_s + R + d \left[\frac{\rho_1}{\rho_2} (K_1\theta + K_2\theta^3) \sin \alpha \cos \varphi \right] + \delta_{\alpha=0} \quad (A3)$$

where r_s is the distance from the center of curvature of the model face to the shock surface.

The angle (ψ) between the velocity vector and the vector normal to the shock wave was determined from this equation and the vector equation

¹The term $(\delta/d)_{\alpha=0}$ is approximately a constant over the face of the model since, over a wide range of flight conditions, the shock envelope at $\alpha = 0$ is nearly concentric with the spherical face for the Apollo configuration.

[REDACTED] **SECRET** [REDACTED]

$$\cos \psi = \frac{\nabla D \cdot V}{|\nabla D| |V|} \quad (A4)$$

The details of the operation on equation (A3) and the subsequent simplification are tedious and will not be reproduced here. The results are

$$\cos \psi = \frac{\left[(-\sin \alpha \sin^2 \theta \cos^2 \varphi - \cos \alpha \cos \theta \sin \theta \cos \varphi)(K_1 \theta + K_2 \theta^3) \right] + \left\{ \left[\frac{r_s - (R + \delta_{\alpha=0})}{r_s} \right] \left[(K_1 + 3K_2 \theta^2)(\sin \alpha \cos^2 \varphi \cos \theta \sin \theta - \cos \alpha \sin^2 \theta \cos \varphi) + (\sin \alpha \sin^2 \varphi)(K_1 \theta + K_2 \theta^3) \right] \right\}}{\left\{ (\sin^2 \theta \cos^2 \varphi)(K_1 \theta + K_2 \theta^3)^2 + \left[\frac{r_s - (R + \delta_{\alpha=0})}{r_s} \right]^2 \left[(K_1 + 3K_2 \theta^2)^2 (\sin^2 \theta \cos^2 \varphi) + (K_1 \theta + K_2 \theta^3)^2 (\sin^2 \varphi) \right] \right\}^{1/2}} \quad (A5)$$

The above equation was programmed for an IBM 7090 computer to solve for ψ .

With the angle between the free-stream vector and the normal to the shock known, the air properties behind the shock wave were calculated for various values of θ and φ by using the oblique shock-wave relations. The predictions of reference 5 were then used to compute the radiant intensity of the equilibrium air just behind the shock at the various values of θ and φ .

For the properties on the body surface, the modified Newtonian pressure coefficient was assumed to hold,² and the gas properties were computed for the same values of θ and φ assuming isentropic flow from the model stagnation point. The radiant intensity was again calculated from reference 5.

The total radiation W , was then determined by numerically integrating the radiant intensity over the shock-layer volume. The numerical integration procedure was as follows.

The shock layer was divided into a large number of volume elements of roughly cubical shape, each element extending from the shock surface to the body surface. The radiant intensity, I , as calculated by the above procedure, was assumed constant on the shock surface and on the body surface of each element.

²Reference 10 shows that this assumption holds within approximately 10 percent.

[REDACTED]

Further, the radiant intensity was assumed to vary linearly between the shock surface and body surface of each element along lines normal to the body surface. Within the framework of these assumptions, the radiation from each volume element is

$$W_{EL} = \frac{I_S + I_B}{2} \delta_{EL} dA \quad (A6)$$

and the total radiation is

$$W = \Sigma W_{EL} \quad (A7)$$

This value was normalized by dividing it by the value of W for $\alpha = 0$, computed in the same fashion for the same test condition. The results were plotted as a function of α to define the curves on figures 9 and 10.

An auxiliary computation was used to determine the roll-angle eclipsing factor from these calculations. The expression for the radiation from each element was written

$$W_{ELseen} = \frac{I_S + I_{PS}}{2} (\delta - \delta_{ECL}) dA \quad (A8)$$

Then

$$W_{seen} = \Sigma W_{ELseen} \quad (A9)$$

and the eclipsing function is

$$\epsilon(\varphi, \alpha) = \frac{W_{seen}}{W} \quad (A10)$$

REF ID: A60000

REFERENCES

1. Seiff, Alvin: A Progress Report on the Ames Hypervelocity Free-Flight Facilities and Some of the Current Research Problems Being Studied in Them. AIAA paper no. 63-162.
2. Curtis, John S.: An Accelerated Reservoir Light-Gas Gun. NASA TN D-1144, 1962.
3. Liepmann, H. W., and Roshko, A.: Elements of Gasdynamics. John Wiley and Sons, N. Y., 1957.
4. Page, William A., Canning, Thomas N., Craig, Roger A., and Stephenson, Jack D.: Measurements of Thermal Radiation of Air From the Stagnation Region of Blunt Bodies Traveling at Velocities up to 31,000 Feet Per Second. NASA TM X-508, 1961.
5. Kivel, B., and Bailey, K.: Tables of Radiation from High Temperature Air. Avco-Everett Res. Rep. 21, 1957.
6. Canning, Thomas N., and Page, William A.: Measurements of Radiation From the Flow Fields of Bodies Flying at Speeds up to 13.4 Kilometers Per Second. Paper presented to the Fluid Mechanics Panel of AGARD, Brussels, Belgium, April 1962.
7. Kaattari, George E.: Shock Envelopes of Blunt Bodies at Large Angles of Attack. NASA TN D-1980, 1964.
8. Givens, John J., Canning, Thomas N., and Bailey, Harry E.: Measurements of Spatial Distribution of Shock-Layer Radiation for Blunt Bodies at Hypersonic Speeds. NASA TM X-852, 1963.
9. Wick, Bradford H.: Radiative Heating of Vehicles Entering the Earth's Atmosphere. Paper presented to the Fluid Mechanics Panel of Advisory Group for Aeronautical Research and Development, Brussels, Belgium, April 1962.
10. Jones, Robert A.: Experimental Investigation of the Overall Pressure Distribution, Flow Field, and Afterbody Heat-Transfer Distribution of an Apollo Reentry Configuration at a Mach Number of 8. NASA TM X-813, 1963.

03:12: [REDACTED]

03

[REDACTED]

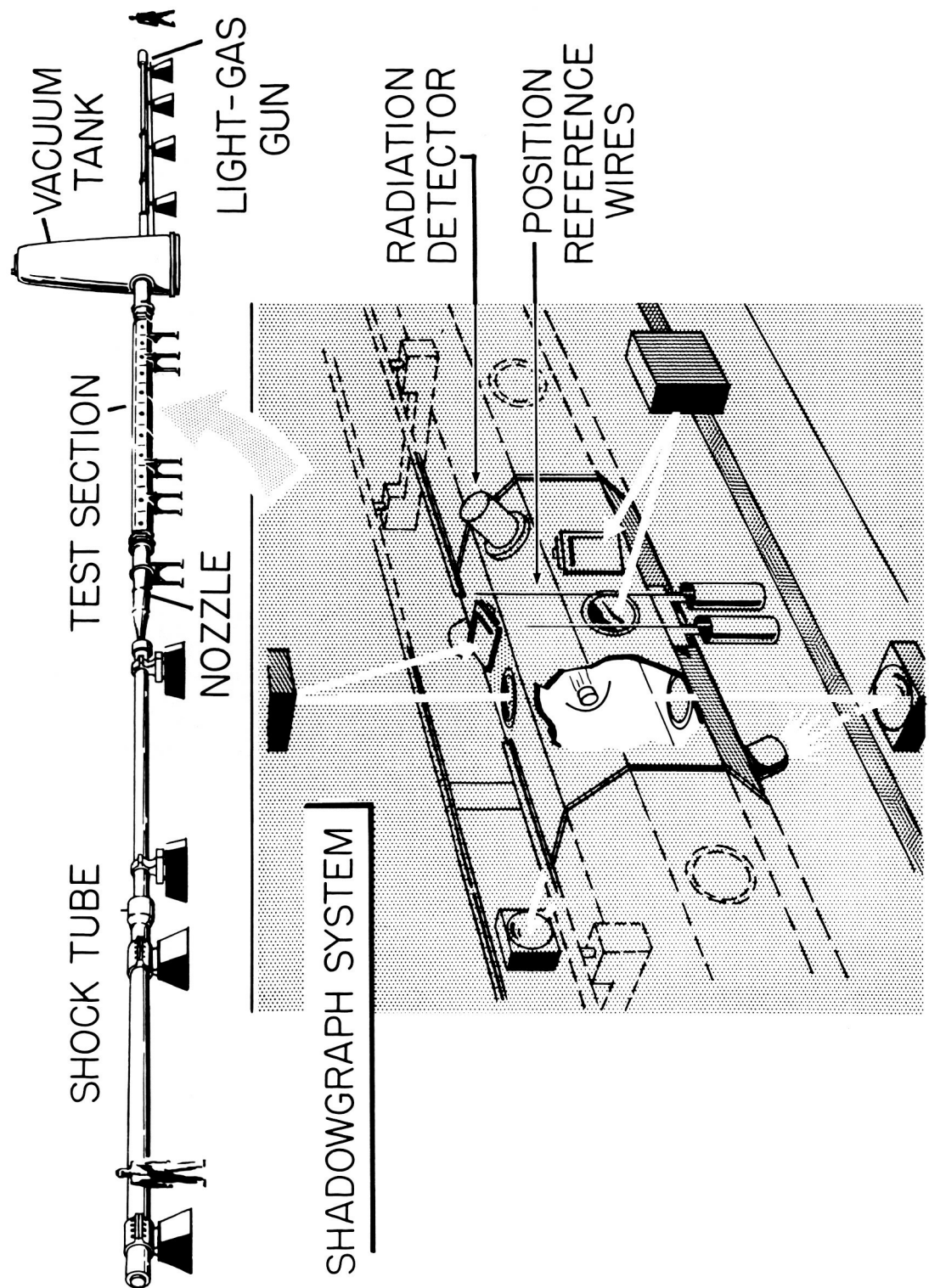
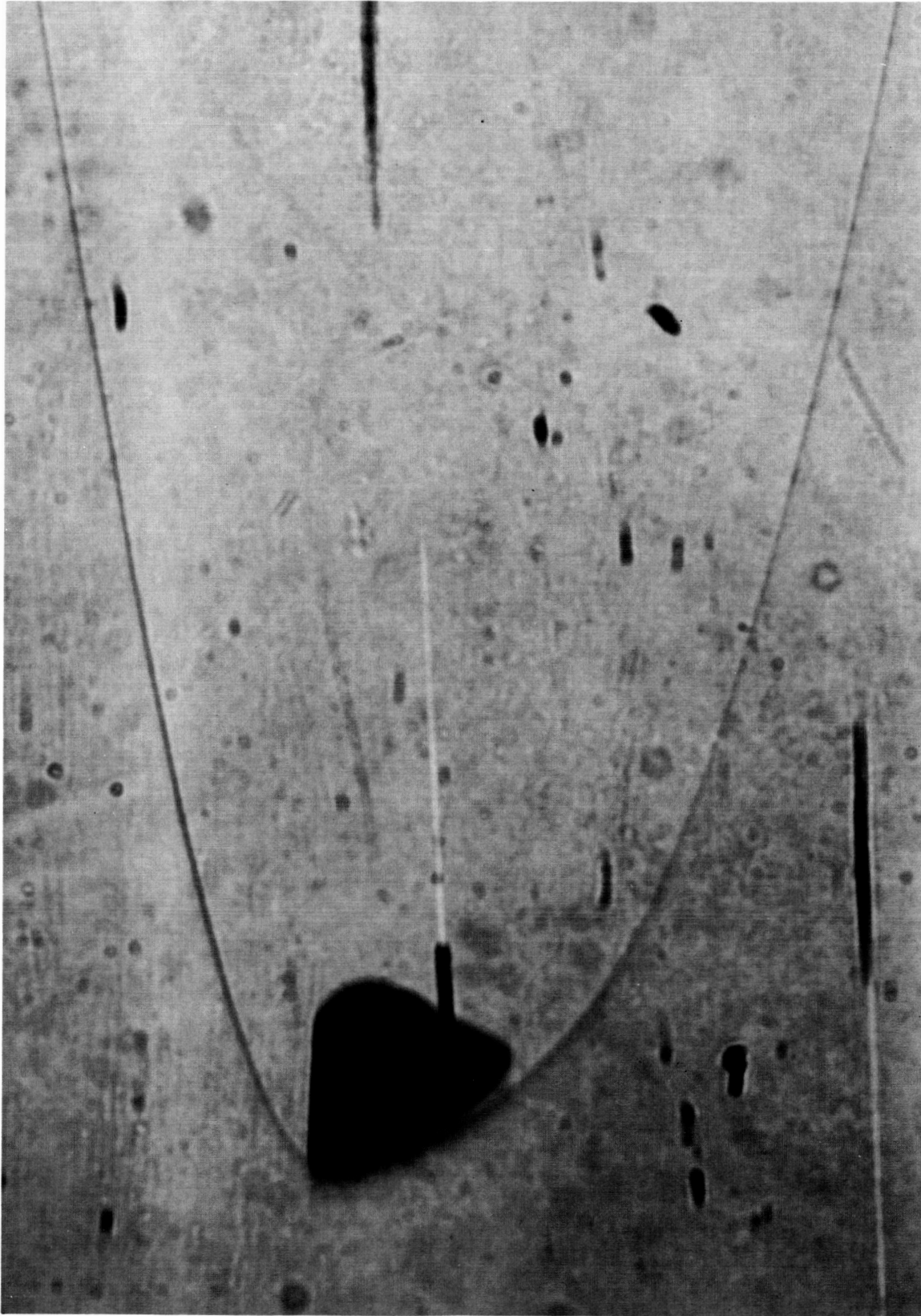


Figure 1.- Schematic drawing of prototype hypersonic free-flight facility.

A-29948-15



A-29925

Figure 2.- Shadowgraph of model in flight; $V = 22,480$ ft/sec, $p_{\infty} = 167$ lb/ft², $\alpha = 27.5^{\circ}$. (The markings on the photo are from the tunnel window.)

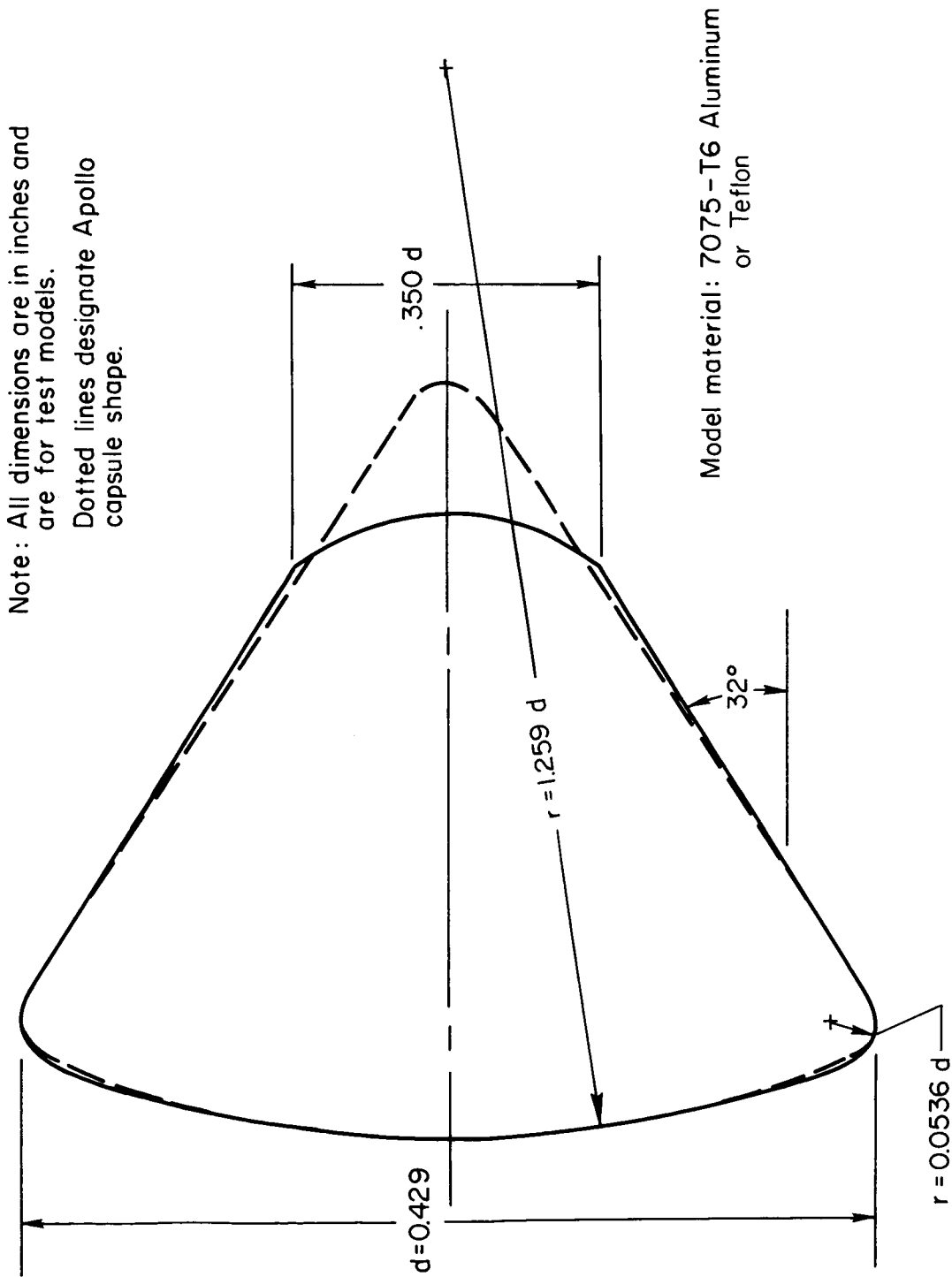
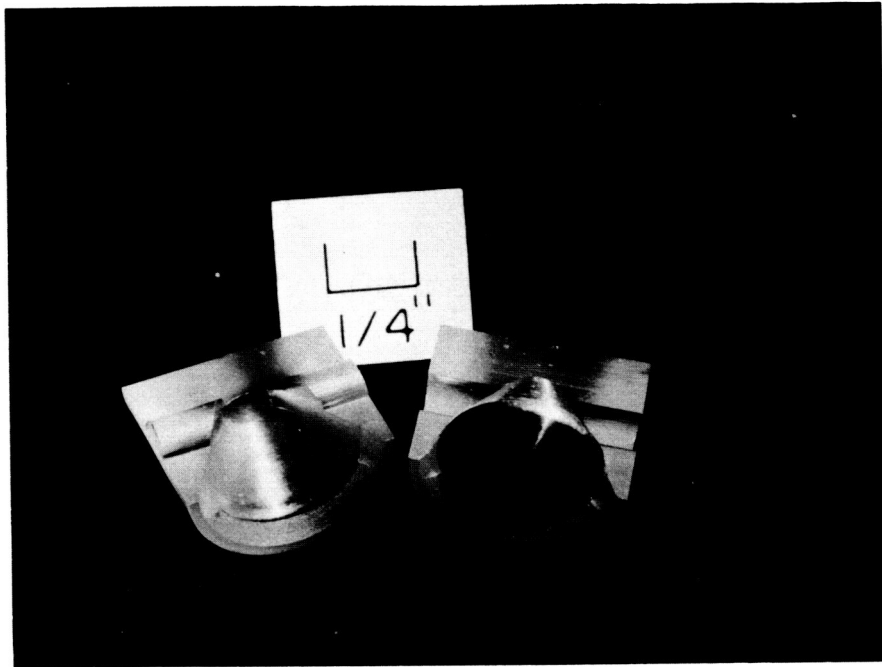


Figure 3.- Sketch of models used in these tests.

03712

03



A-31151

Figure 4.- Model and sabot.

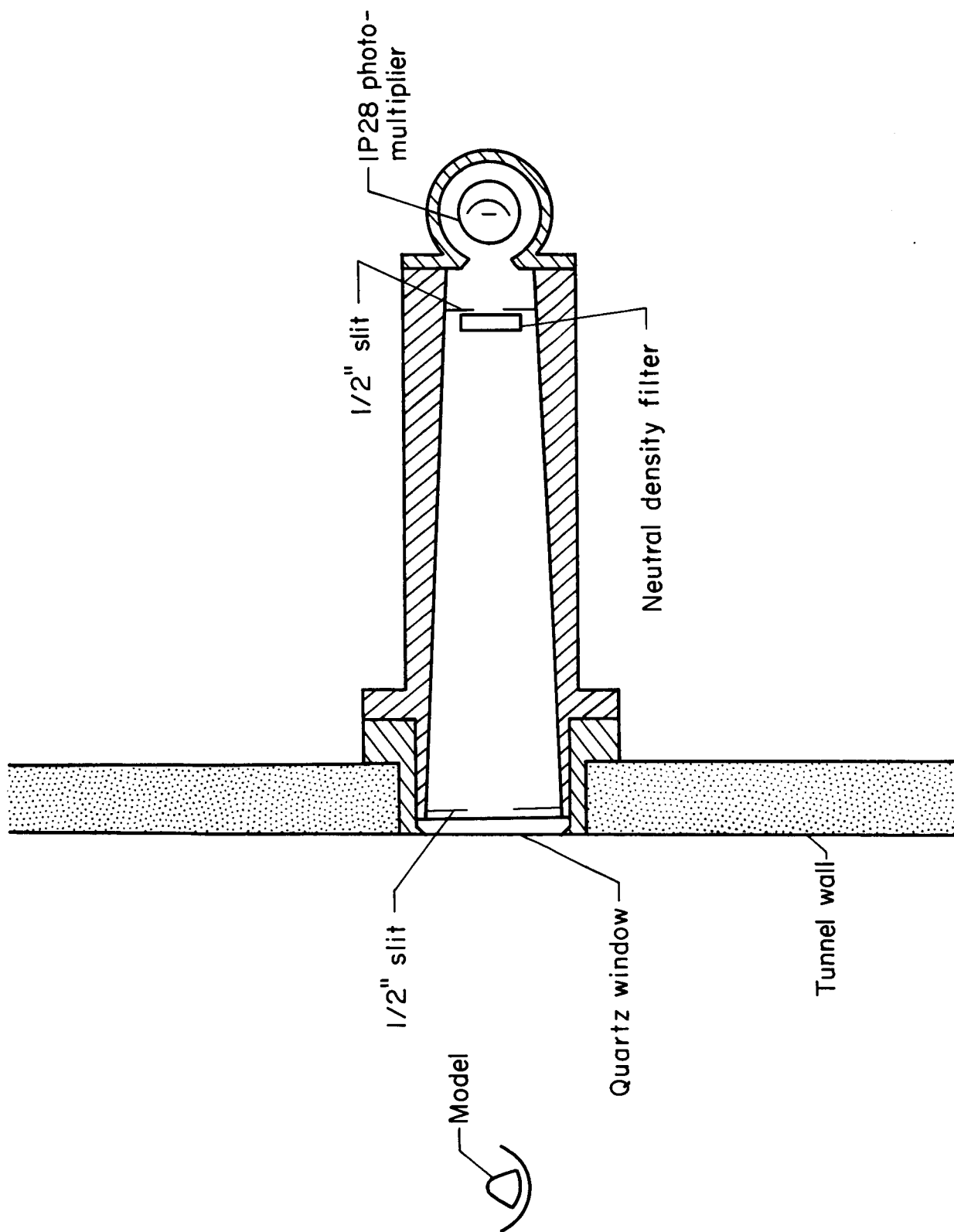


Figure 5.- Schematic drawing of radiation measuring station.

03713

8

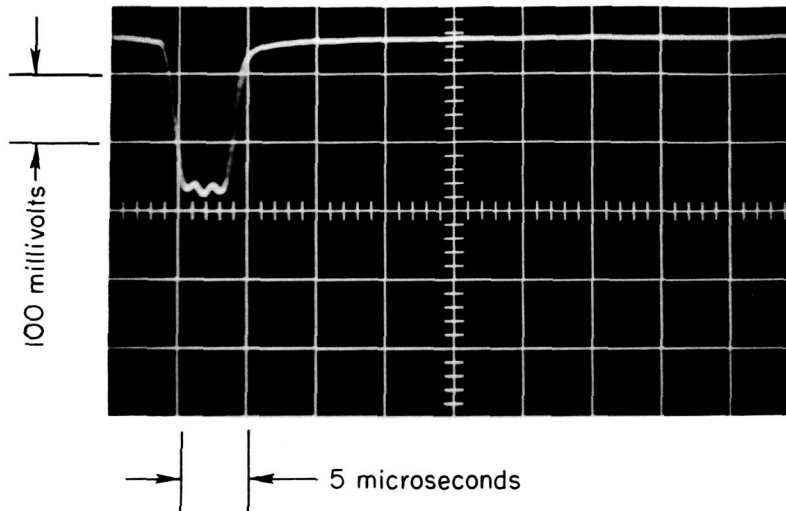
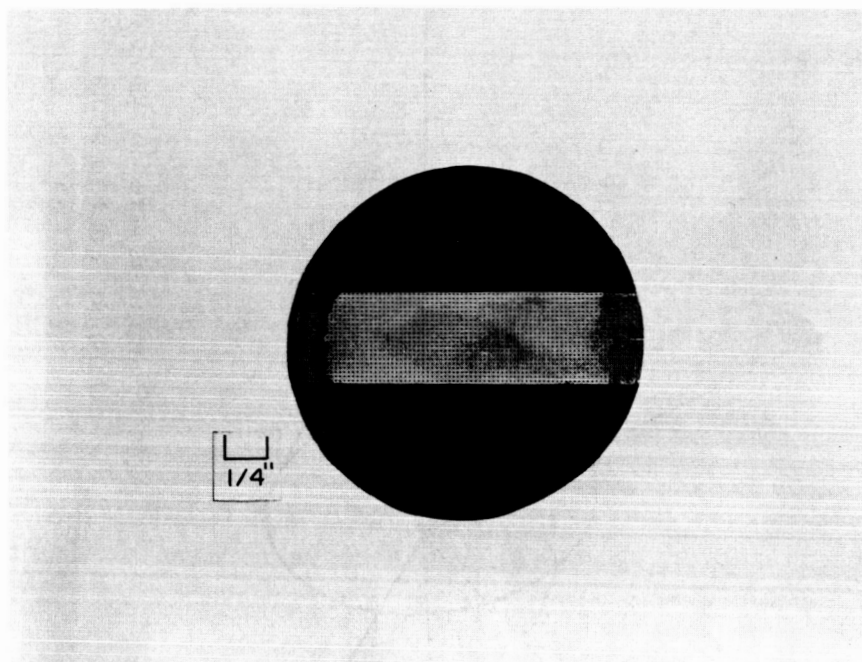


Figure 6.- Typical oscillogram showing radiometer output.

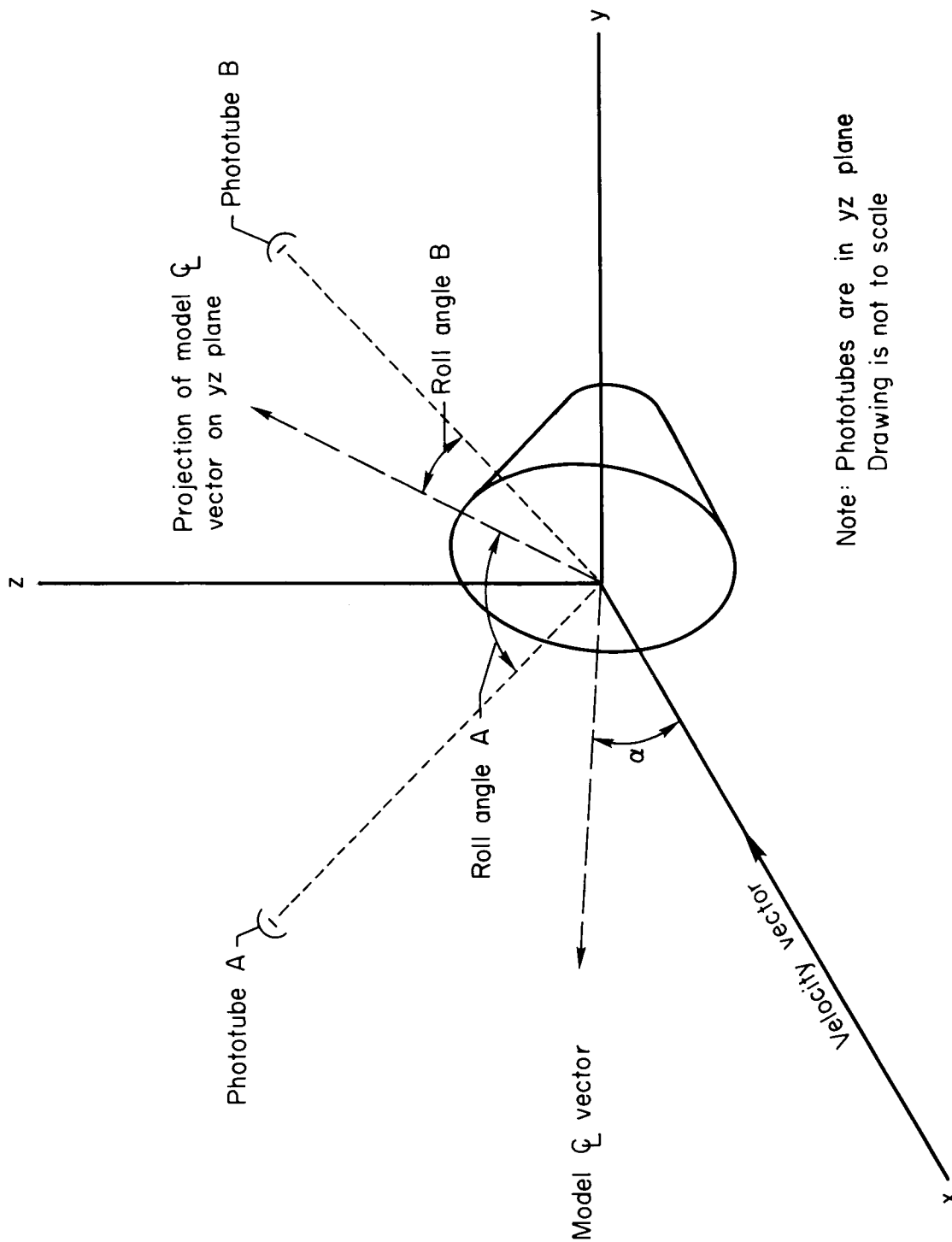


RECEIVED



A-31128

Figure 7.- Screen-type neutral density filter.



Note: Phototubes are in yz plane
Drawing is not to scale

Figure 8.- Definition of roll angle and angle of attack of model.

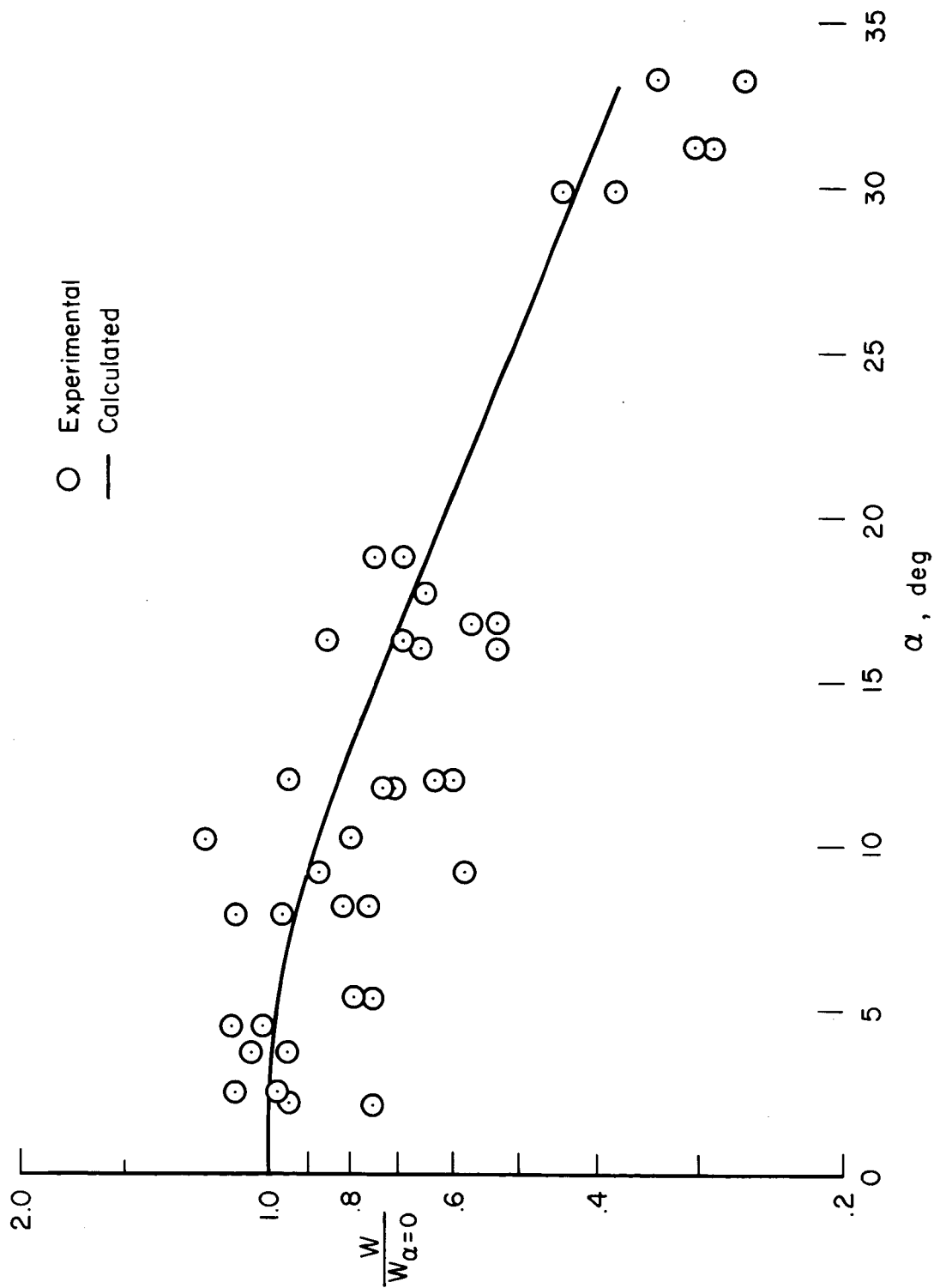


Figure 9.- Relative front-face radiative heat load as a function of angle of attack; $V = 23,000$ ft/sec.

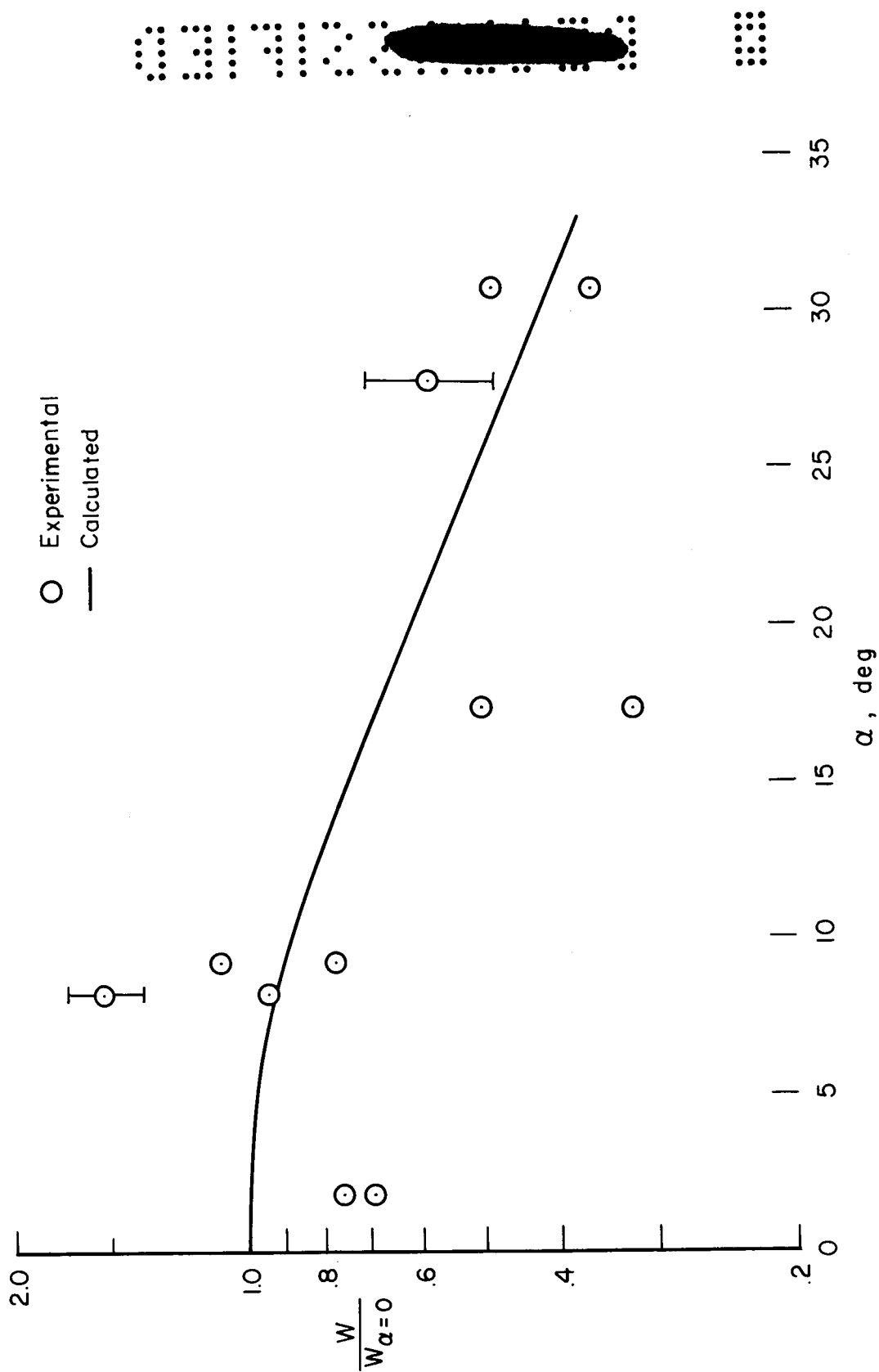


Figure 10.- Relative front-face radiative heat load as a function of angle of attack; $V = 35,000$ ft/sec.



CONFIDENTIAL

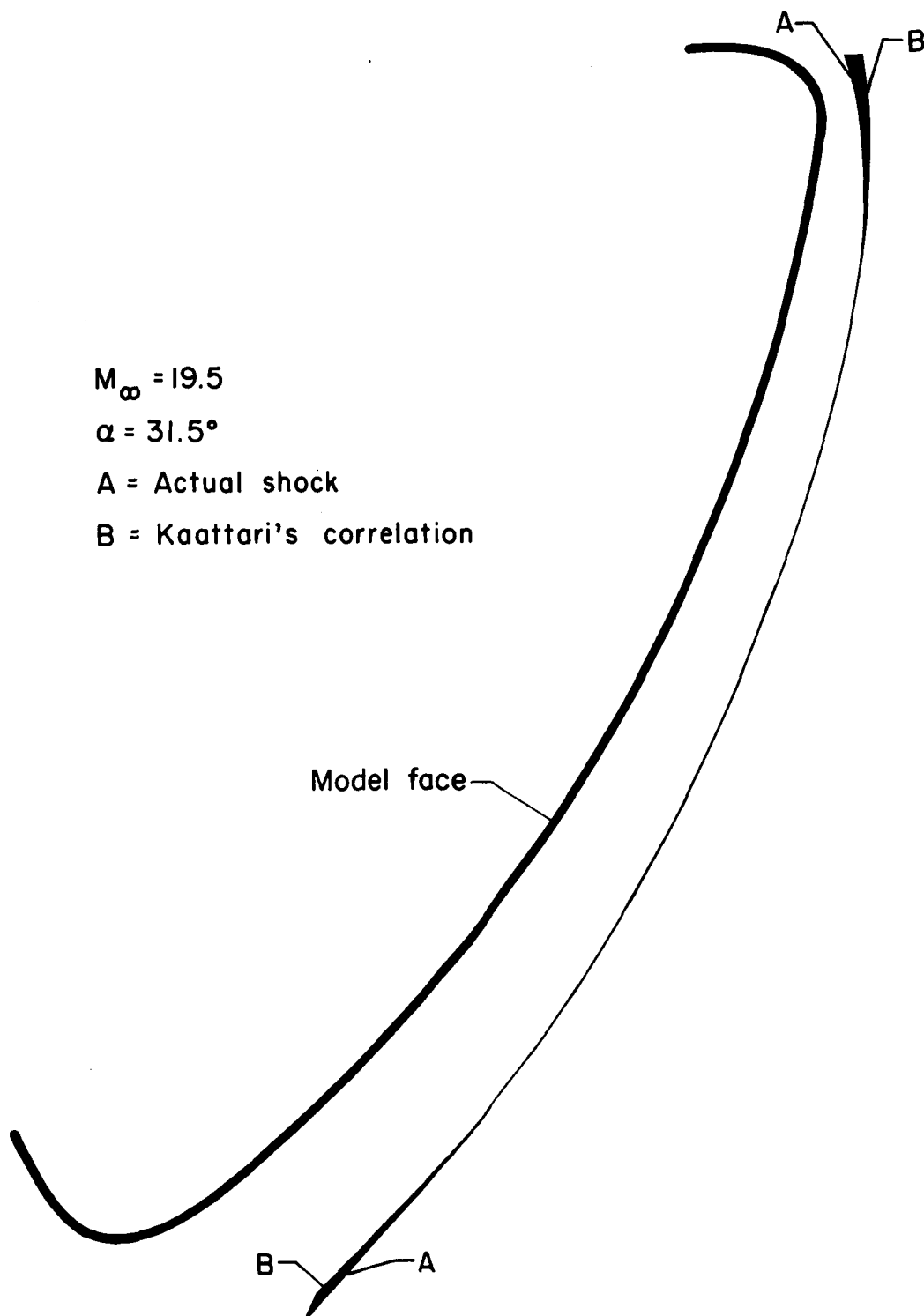


Figure 11.- A comparison of a shock-wave shape derived from an experimental shadowgraph with a shock-wave shape computed by the methods of reference 7.

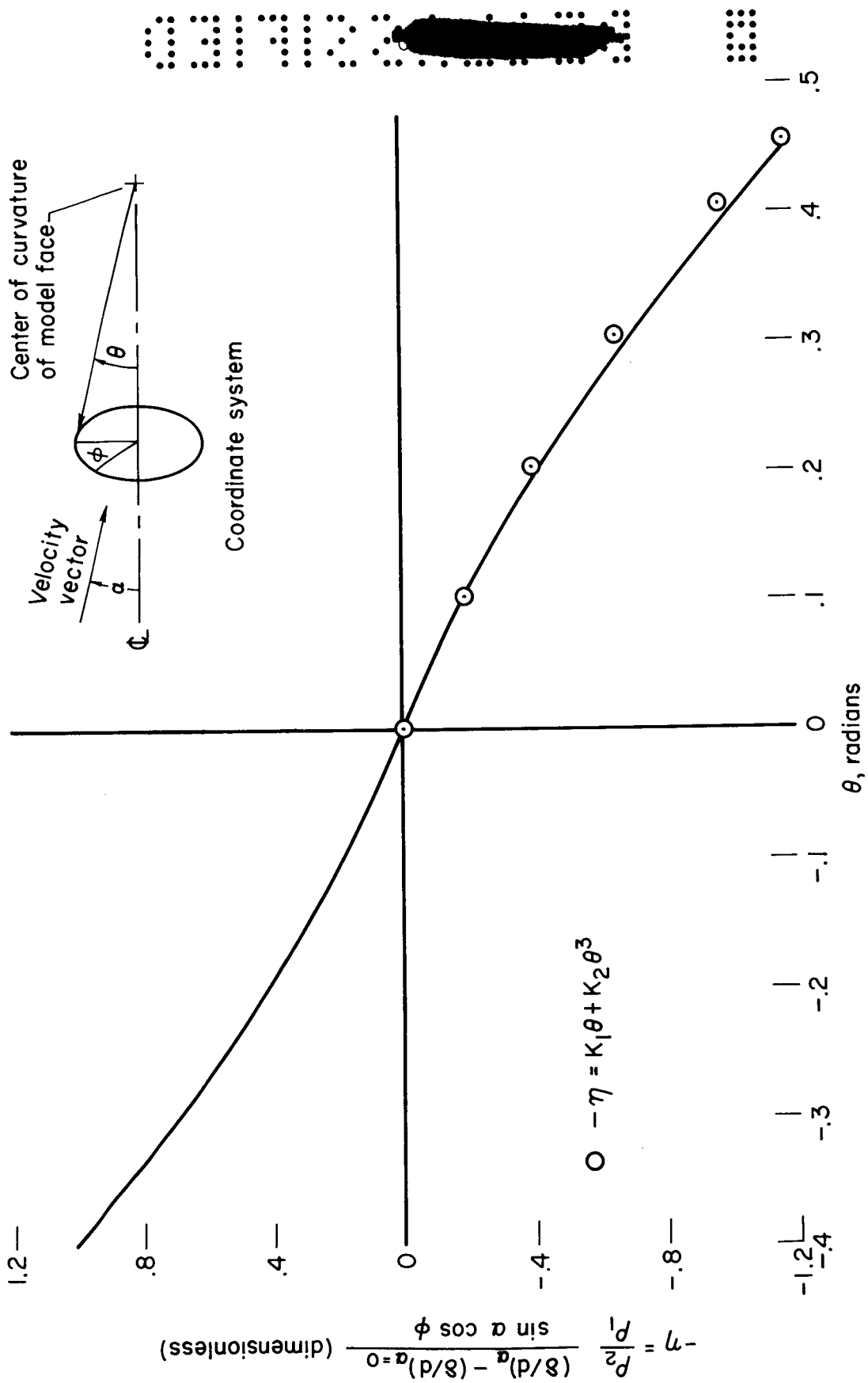


Figure 12.- Correlation of bow shock wave shape data from reference 7.